The 2017, Mw 3.9, Ischia Earthquake (Southern Italy): Source mechanism from the modelling of seismic, geodetic, and geological data and relation to the volcano resurgence mechanism

Sahar Nazeri[1], Aldo Zollo[1], Guido Maria Adinolfi[1], Ortensia Amoroso[2], and Matteo Picozzi[1]

[1]Department of Physics "E. Pancini", University of Naples Federico II, Naples, Italy
[2]Department of Physics "E.R. Caianiello", Università degli Studi di Salerno, Fisciano, Salerno, Italy.

November 23, 2022

Abstract

The moderate earthquake occurred at the volcanic island of Ischia, south-west of Naples (Italy) caused several buildings collapse, two victims, and several tens of injured people. This event generated a large amplitude ground shaking and long-lasting S-wave signal, longer than those expected for an earthquake. To investigate the event rupture complexity and its radiated wave field, we used finite-fault modelling to invert the near-source (< 1 km epicentral distance), three-component velocity records of the accelerometric station (IOCA), and searched for the best-fit kinematic rupture parameters. This analysis showed that the rupture nucleated at about 600 m west of IOCA and 1.1 km depth, along a 1 km, NW-SE striking fault (thrust-strike slip with right-lateral component), with a rupture velocity 0.8 km/s. The retrieved rupture model coupled with multi-path reverberations effects related to a thin, low-velocity near-surface volcanic sedimentary layer, allowed us to explain the observed long ground motion duration and the large amplitudes recorded all over the island. The actual fault location, mechanism, and the spatial correlation between the simulated peak ground motion zone and the area where the maximum vertical displacement has been determined by DInsar images suggest that the latter is associated with strong-shaking locally generated by land-slide phenomena caused by co-seismic slip. Our source model is consistent with the earthquake located near the border of the caldera resurgent block, which is likely still active, where mass rock creeps evolved into widespread collapses at NW of Monte Epomeo.

Hosted file

essoar.10504375.1.docx available at https://authorea.com/users/542727/articles/601041-the-2017-mw-3-9-ischia-earthquake-southern-italy-source-mechanism-from-the-modelling-of-seismic-geodetic-and-geological-data-and-relation-to-the-volcano-resurgence-mechanism

Hosted file

jgrse-nazeri-et al-si.docx available at https://authorea.com/users/542727/articles/601041-the-2017-mw-3-9-ischia-earthquake-southern-italy-source-mechanism-from-the-modelling-of-seismic-geodetic-and-geological-data-and-relation-to-the-volcano-resurgence-mechanism

1 **The 2017, Mw 3.9, Ischia Earthquake (Southern Italy): Source mechanism from the modelling**

2 **of seismic, geodetic, and geological data and relation to the volcano resurgence mechanism**

3 **Sahar Nazeri[1], Aldo Zollo[1], Guido Maria Adinolfi[1], Ortensia Amoroso[2] and Matteo Picozzi[1]**

4 [1] Department of Physics "E. Pancini", University of Naples Federico II, Naples, Italy.

5 [2] Department of Physics "E.R. Caianiello", Università degli Studi di Salerno, Fisciano, Salerno,

6 Italy.

7

8 **Key Points:**

9 • The rupture complexity and source geometry of the 2017 Ischia earthquake (Italy) is

10 investigated.

11 • The finite-fault model is implemented to invert the near-source velocity records.

12 • The results show that the rupture mechanism is thrust-strike (right lateral) slip and

13 propagated north-west south-east direction.

14   **Abstract**

15   The moderate earthquake occurred at the volcanic island of Ischia, south-west of Naples (Italy)

16   caused several buildings collapse, two victims, and several tens of injured people. This event

17   generated a large amplitude ground shaking and long-lasting S-wave signal, longer than those

18   expected for an earthquake. To investigate the event rupture complexity and its radiated wave

19   field, we used finite-fault modeling to invert the near-source (< 1 km epicentral distance),

20   three-component velocity records of the accelerometric station (IOCA), and searched for the

21   best-fit kinematic rupture parameters. This analysis showed that the rupture nucleated at

22   about 600 m west of IOCA and 1.1 km depth, along a 1 km, NW-SE striking fault (thrust-strike

23   slip with right-lateral component), with a rupture velocity 0.8 km/s. The retrieved rupture

24   model coupled with multi-path reverberations effects related to a thin, low-velocity near-

25   surface volcanic sedimentary layer, allowed us to explain the observed long ground motion

26   duration and the large amplitudes recorded all over the island. The actual fault location,

27   mechanism, and the spatial correlation between the simulated peak ground motion zone and

28   the area where the maximum vertical displacement has been determined by DInsar images

29   suggest that the latter is associated with strong-shaking locally generated by land-slide

30   phenomena caused by co-seismic slip. Our source model is consistent with the earthquake

31   located near the border of the caldera resurgent block, which is likely still active, where mass

32   rock creeps evolved into widespread collapses at NW of Monte Epomeo.

33

34

35   **1 Introduction**

36   On August 21, 2017, a moderate size earthquake, Mw 3.9 (INGV bulletin), had struck the

37   Casamicciola town in the northwestern sector of the Ischia island generating few casualties and

38   damages in a limited area. Historical information reports that before the 19th century, the

39   island was affected by various moderate magnitude events with relatively high macroseismic

40   intensity (i.e., IMCS>V; Mercalli-Cancani-Siberg scale) (Figure 1). Then, in 1881 and 1883 two

41   destructive events occurred in the same location of the 2017 event, the area of Lacco Ameno

42   and Casamicciola, with more than a hundred of fatalities and widespread building collapses (Del

43   Gaudio et al., 2019). The 1883 earthquake, with an estimated magnitude between 4.3 and 5.2,

44   and a depth between 1 and 2 km (CPTI15, Luongo et al., 2006), reached a macroseismic

45   intensity IMCS = X at the epicenter in the town of Casamicciola.

46   After the 2017 earthquake, several studies have been proposed with the aim to describe the

47   earthquake source characteristics and its effects. De Novellis et al. (2018) investigated the 2017

48   earthquake mechanism by exploiting seismological, GPS and Sentinel-1 and COSMO-SkyMed

49   differential interferometric synthetic aperture radar coseismic measurements. The 2017

50   mainshock and its five aftershocks have been located using the probabilistic location method of

51   Lomax et al. (2000) using the available P- and S-phase pickings. To locate the mainshock only

52   the P-wave arrivals at the three closest stations installed in the island have been used since the

53   signal saturation prevents the accurate reading of the first S-arrival. A 3D velocity model built

54   upon previous tomographic studies of the extended Neapolitan volcanic area has been used for

55   the computation of theoretical arrival times. It should be noted that the first P-arrivals at

56   coastal stations (distances larger than 10-20 km) are primarily head waves from the shallow

57 crustal discontinuities, among which, the main one is the interface separating the volcanic

58 sediments and the limestone formation, whose morphology and depth is not known with

59 accuracy and not included in 3D unified velocity model of D'Auria et al. (2008). This uncertainty

60 on the velocity model may seriously affect the earthquake location and focal mechanism

61 determination.

62 Braun et al. (2018) evaluated the 2017, Ischia earthquake location by combining the P-wave

63 particle motion, rotated spectra, and S-minus-P time observed at IOCA station, yielding a

64 hypocenter depth of 2 km and a location 0.5-1 km south-west of IOCA; leading to the same

65 epicentral area of the 1883 devastating earthquake. The epicenter locations proposed by Braun

66 et al. (2018) and De Novellis et al. (2018) are in good agreement, while their depth estimates

67 differ of about 1 km.

68 Differently from location, several significantly discrepant solutions have been proposed for the

69 focal mechanism of the Ischia mainshock; mainly derived from the inversion of P-wave

70 polarities at local distances or moment tensor inversion at regional distances (De Novellis et al.,

71 2018; Braun et al., 2018). A comprehensive review of the different published solutions is

72 provided by Braun et al. (2018), who further applied the combined spectral and time domain

73 method of Cesca et al. (2013) to determine the earthquake moment tensor. These authors

74 provided a solution with both large negative isotropic and compensated linear vector dipole

75 (CLVD) components, which led them to suggest the occurrence of a complex rupture process

76 characterized by an initial shallow normal-faulting event that triggered a subsequent shallow

77 underground collapse.

78   Based on the INGV hypocenter depth and focal mechanism solutions, De Novellis et al. (2018)

79   proposed that the 2017 Ischia earthquake mechanism has been generated by an E-W striking,

80   South dipping normal fault, with a hypocenter located at a depth of 800 m. In that study, the

81   joint inversion of DInSAR and GPS coseismic measurements led to estimate the origin of the slip

82   distribution in a main patch (maximum slip amplitude 14 cm) located at the center of the fault

83   plane at hypocentral depth (De Novellis et al., 2018). The strike of the fault has been found

84   roughly consistent with an apparent aftershock alignment along the E-W direction and with the

85   computed focal mechanism from regional seismic waveforms. However, the same authors

86   pointed out a main difference between the seismological and geodetic modelling solutions,

87   with an important strike-slip component of the first which is not present in the second one.

88   While the prompt availability of DInSar data allowed to rapidly provide estimates of source

89   location and mechanism for the Ischia earthquake, it is worth noting that DInSar data modelling

90   is based on the assumption that the detected ground displacement is primarily generated by

91   the co-seismic contribution of the causative earthquake fault. Recently, Albano et al. (2018)

92   revisited the DInSar data relevant to the Ischia event and investigated the possible contribution

93   of earthquake-induced landslides to the detected ground displacements. Based on the limit

94   equilibrium method, they estimated the spatial extent of the earthquake-induced landslides

95   and the associated probability of failure. The results of this study led the authors to conclude

96   that "the observed ground displacement field is the combination of both fault slip and surficial

97   sliding caused by the seismic shaking" (Albano et al., 2018).

98   The 2017, Ischia earthquake impact on buildings and structures of the island has been assessed

99   through a series of surveys conducted immediately after the event by the RELUIS-DPC team

100   (DPC, 2017) and INGV-ENEA team (Azzaro et al., 2017). Del Gaudio et al. (2019) reviewed the in-

101   situ observations of the damage state of masonry and RC buildings in the epicentral area and

102   matched them with the simulated damage scenarios built upon the data from the 15th national

103   census of the population and dwellings (ISTAT) converted into vulnerability classes. The latter

104   are expressed according to the classification of the European Macrosismic Scale (EMS-98). In

105   evaluating the seismic damage scenarios, the intensity shake map of the 2017 Ischia event is

106   reconstructed using an interpolation method based on QUEST macro-seismic survey data

107   (Azzaro et al., 2017). The map shows an anisotropic distribution of intensities, with highest

108   values in the SE and SW directions from the epicentral area, with the former having a more

109   pronounced and extended lobe.

110   The present work has been primarily motivated by the availability of a high-quality strong-

111   motion record in the near-source distance range (less than a 1 km epicentral distance) of the

112   2017, Ischia earthquake. Our refined modelling of the high-frequency signals (up to 3 Hz)

113   brought new insight on both extended fault and rupture mechanism. Indeed, previous

114   modelling of the IOCA waveform in De Novellis et al. (2018) and Braun et al. (2018), mainly

115   concerned the low frequency band (0.1-2 Hz) and assumed a point-source earthquake

116   approximation.

117   The anomalous duration (about 4 sec) of the large amplitude, velocity and displacement

118   waveforms observed at IOCA station (Figure 2), as compared to the expected (about 1 sec)

119   source duration of similar size events (Wells & Coppersmith, 1994), suggests a possible coupling

120   effect of the very shallow earthquake rupture and wave propagation across the near-surface

121 sedimentary layers which could have contributed to amplify and extending the ground shaking

122 duration and hence the event damaging effects.

123 We mainly adopted a two-step modelling procedure of the strong motion records assuming,

124 first, a point-source mechanism, and then a finite-fault model where a forward modelling is

125 combined with a non-linear inversion technique to retrieve the kinematic rupture model

126 information (e.g., rupture length and orientation, slip distribution along the strike and average

127 rupture velocity) and therefore it allows generating a synthetic shake map. In addition, the

128 rupture model has been validated through the GPS data modelling and peak ground velocity

129 prediction as converted from intensity contours.

130 The retrieved rupture model coupled with multi-path reverberations effects related to a thin,

131 low velocity near-surface volcanic sedimentary layer, allows to explain the observed ground

132 motion duration at IOCA and strong shaking amplitudes and intensities recorded all over the

133 island. The joint interpretation of seismic, geodetic, and geological structural data point to an

134 earthquake triggering process related to long-term volcano resurgence phenomena.

135 **2 Geological and Volcanological Setting of Ischia Island**

136 Ischia belongs, together with volcanic islands of Procida and Vivara along a SW direction from

137 the caldera of Campi Flegrei, to the Phlegraean volcanic district that was built since Pliocene as

138 a result of the extensional deformation that involved the Tyrrhenian margin of Apennines chain

139 and generated the graben of Campanian Plain (Gillot et al., 1982; Vezzoli, 1988).

140 Ischia is an active volcano that rises above the seafloor for over 1000 m (Bruno et al., 2002),

141 whose natural hazard is connected to its magmatic system and the related interdependent

142   phenomena (Selva et al., 2019), as testified by the large number of eruptions occurred in

143   historical times with the most recent of the 1302 AD (Vezzoli, 1988; Iacono, 1996).

144   Nowadays, the island is interested by an active hydrothermal system with widespread

145   fumaroles and thermal springs (Chiodini et al., 2004; Di Napoli et al., 2011 and references

146   therein) and seismic activity.

147   The oldest existing rocks on the Island of Ischia show an age of ca. 150 ky as evidenced by the

148   K/Ar radiometric dating method (Vezzoli, 1988). By geological, volcanological, and petrological

149   studies, in the last 55 k.y. of history, the volcanic system has been extensively restored (Civetta

150   et al., 1991) as result of periods dominated by different differentiation processes related to the

151   injection of new magmas (less differentiated) into a shallow reservoir (De Vita et al., 2010). The

152   first period (55–33 k.y.; Gillot et al., 1982; Vezzoli, 1988) was dominated by the Monte Epomeo

153   Green Tuff eruption that formed a volcanic caldera located at the center of the island. Since 33

154   ka, the Ischia volcanic system experienced an asymmetric resurgence of the caldera floor due to

155   the injections of new magma, forming the Monte Epomeo block (Orsi et al., 1991).

156   The complex volcano-tectonic framework of Ischia is related to the two regional fault systems

157   with NE-SW- and NW-SE-trending, whose intersection controls the structure of the island

158   (Acocella & Funiciello, 1999; De Vita et al., 2010) and it was responsible for shallow-depth

159   magma emplacement and extrusion (Acocella et al., 2001) during the Pliocene-Quaternary

160   extensional phases. The reactivation of regional faults and the newly generated fault activity,

161   directly connected with volcano-tectonism, produced the resurgence of the irregularly

162   octagonal shape block of Monte Epomeo (Orsi et al., 1991; Acocella & Funiciello, 1999). The

163   block displays an asymmetrical structure due to a variably and irregular growth that caused a

164   tilt along an NE-SW trending horizontal axis and a larger uplift in the NW part of the caldera

165   area. In this area, the deformation has been accommodated by inward-dipping, high-angle

166   reverse faults, whose trends range between NE-SE to NW-SE through NS directions, especially

167   at edges of the most uplifted block.   Subsequently, gravitational instability phenomena

168   produced late outward dipping normal faults, that cut the former tectonic features (Chiodini et

169   al., 2004; De Vita et al., 2006). The area located to the E and SE of this block has been

170   downthrow by several normal faults (N-S-, NE-SW-, and NW-SE–trending) through a series of

171   differentially displaced blocks connected with the resurgent area of Monte Epomeo (De Vita et

172   al., 2010).

173   Although several hypotheses have been proposed for the resurgence of Monte Epomeo block,

174   the injection of new batches of magma towards shallow depths is the most accepted triggering

175   mechanism by several authors (e.g., among others, Rittmann, 1930; Rittmann & Gottini, 1980;

176   Orsi & Chiesa, 1988; Orsi et al., 1991; Luongo et al., 1995; Carlino et al., 2006).

177   The last 10 ky of the Ischia volcanic system was characterized by alternating periods of

178   quiescence and periods of intense volcanism, especially at ca. 5.5 ky and over the past 2.9 ky

179   (De vita et al., 2010). Structural and volcanological evidences show that the volcanism in this

180   period was strongly influenced by the resurgence mechanism, which allowed new upward

181   impulses of magma mainly in the eastern area of the island (Orsi et al., 1991; Marotta, 2001). In

182   this sector, located outside the resurgent block, the magmatic activity produced local stress

183   field likely capable of activating pre-existent regional faults developed in the extensional regime

184   (De Vita et al., 2010). Since the volcanism at Ischia island was discontinuous in the last 33 ka,

185   the magma intrusion, as well as the caldera resurgence, is supposed irregular and intermittent

186   through time (Orsi et al., 1991; Tibaldi & Vezzoli, 1997).

187   The resurgence of Monte Epomeo controlled, not only the volcanic activity, but probably the

188   slope-instability that preceded and followed the emplacement of volcanic products as

189   evidenced by geological data. In fact, in the past 5.5 ka, the volcanic eruptions coexisted with

190   slope failures or mass movements that led to the development of terrigenous landslides

191   deposit (De Vita et al., 2006; Selva et al., 2019).

192   **3 Data and Methodologies**

193   The 2017 Ischia earthquake has been well detected and recorded by INGV seismic stations on

194   the island and on the Italian peninsula up to few hundreds' km far from the epicenter. Although

195   at near-source distances few stations were operating, only the three-component accelerometer

196   IOCA recorded the unsaturated and complete signal radiated from the earthquake. Two further

197   INGV seismometer stations (velocity sensors, i.e., CAI and F09, Figure 1) show clear P-onsets,

198   while the following seismic phases are clipped. Considering the event location reported by INGV

199   network, IOCA is located at few hundred meters North of the epicenter; it measured peak

200   amplitudes in acceleration (PGA) equal to 0.28 g (on both the EW and vertical components),

201   velocity (PGV) of 18.14 cm/s, and displacement (PGD) of 2.32 cm.

202   To model this earthquake, we mainly performed a multi-steps strategy using various data and

203   including different methods and the processing steps as it is presented in the following sections.

204   As a summary first, the three-component waveforms recorded at IOCA have been modelled to

205   determine the rupture kinematic parameters of the 2017 Ischia earthquake using a two-step

206 modelling approach. In the first step, assuming a point-source approximation, the centroid

207 location of the source and its focal mechanism have been constrained by modelling the low-

208 pass filtered (up to 0.5 Hz), early P- and S-wave signals at IOCA station (about 2-seconds after

209 the P-onset). In the second step, a signal time window of four seconds, which includes large

210 amplitude reverberations appearing on the horizontal components and an extended frequency

211 band (up to 3 Hz) have been used to retrieve the parameters of a finite-fault source model

212 (linear rupture): rupture model (uni- or bi-lateral), length, velocity and slip amplitude along the

213 line. Finally, to validate the retrieved rupture model, we compared the predicted and observed

214 ground displacement model inferred from the GPS data, and matched the observed intensity

215 map with synthetic generated peak ground velocity and acceleration.

216 **3.1 Point-Source Approach**

217 Assuming the point-source approximation, the source position and mechanism parameters,

218 have been obtained by inverting the three-component strong motion records at the IOCA

219 station in the time domain. To this purpose, the signals have been band-pass filtered (first order

220 Butterworth filter) in the frequency band (0.05-0.5) Hz to be compliant with the point-source

221 approximation, given the expected kilometric rupture size, depth and wave propagation

222 velocity of shallow sedimentary layers.

223 For the waveform's inversion, we applied the unconstrained, nonlinear Powell's optimization

224 algorithm (Powell, 1983; Tonel, 2020). This technique allows to retrieve the focal mechanism

225 angles (strike, dip and slip) by optimizing a cost function built upon the criteria of both

226 minimizing the Root-Mean Square Deviation (RMSD) and maximizing the Correlation Coefficient

227 (CC) parameter between observed waveform data (A^{obs}) and calculated synthetics (A^{syn}),

228 defined by:

$$RMSD = \sqrt{\frac{1}{N} \sum_{i=1}^{N} \left\| A_i^{obs} - A_i^{syn} \right\|^2} \tag{1}$$

$$CC = \frac{1}{N-1} \sum_{i=1}^{N} \left(\frac{\overline{A_i^{obs} - \mu_{A^{obs}}}}{\sigma_{A^{obs}}} \right) \left(\frac{A_i^{syn} - \mu_{A^{syn}}}{\sigma_{A^{syn}}} \right) \tag{2}$$

229 where N indicates total number of points in the discrete waves, and μ and σ are the mean and

230 standard deviation of the signals, respectively.

231 The Powell's inversion method in an iterative procedure performs multi-dimensional

232 optimization to search for a local minimum in the model parameter space of a real-valued

233 function of observed and theoretical data computed from a given vector of model parameter

234 values. The search is initialized by setting a number of initial vectors of parameter values.

235 Typically, the initial search vectors are simply the normal parameter values aligned to each

236 model parameter axis. The algorithm establishes a model cost function of the actual model

237 parameter values Q k {\displaystyle Q_{k}} by quadratic interpolation and then minimizes it Q k

238 {\displaystyle Q_{k}} within a trust region with an iterative procedure.

239 Due to the expected strong non-linearity and not-uniqueness of the inverse problem solution,

240 the choice of the initial vector parameter for the Powell' inversion algorithm is relevant. For this

241 reason, we run the inversion using 11 different initial mechanisms (Figure 3c) which included

242 strike-slip, normal, thrust and reverse-oblique fault mechanisms, consistent with the observed

243 pattern of faults in the epicentral area (Acocella & Funiciello, 1999, 2006).

244   Among the tested initial mechanisms, we also considered the INGV (De Novellis et al. 2018)

245   solution and three further mechanisms (Figure S1) resulted from the inversion of first-P- and S-

246   wave polarities at CAI, F09 and IOCA stations and moment tensor inversion of the regional

247   waveforms as well. To obtain these three initial mechanism solutions, we applied different

248   methodologies relying on different pieces of information as explained below.

249   First, combining the information of S-wave polarization (IOCA) and P-wave polarities (IOCA, CAI,

250   F09), we performed a non-linear inversion for studying the earthquake mechanism following

251   Zollo & Bernard (1991). The posterior probability for the strike, dip and rake of the focal

252   mechanism is computed using a Bayesian approach (Lancieri & Zollo, 2008), relying on

253   observational data and a refined flat-layered velocity model retrieved in this work and

254   described later (Figure S2).

255   Also, this analysis is used to constrain the depth and epicentral distance range of the source

256   from station IOCA, consistent with the first P and S arrival time modelling. The origin time of the

257   event has been constrained to the value provided by the INGV bulletin. This analysis gives an

258   earthquake depth range of 300-800 m with epicentral distance of 400-800 m from IOCA.

259   Second, P-wave polarities provided by the Ischia island and Italian peninsula records are also

260   inverted to find the double-couple fault-plane solution that best fits the observed first motions

261   using FPFIT code (Reasenberg & Oppenheimer, 1985, Figure S3). The position of the seismic

262   stations on the focal sphere is calculated using a gradient average model derived from a 1-D

263   regional velocity structure (Scognamiglio et al., 2009), which allows to minimize the take-off

264   angles of seismic P-wave rays by the depth of horizontal interfaces.

265   Finally, the moment tensor solution for the Ischia earthquake has been determined by the Time

266   Domain Moment Tensor (TMDT) full waveform inversion (Dreger, 2003; Dreger & Helmberger,

267   1993). The complete, three-component broad-band displacement waveforms are inverted to

268   estimate a point-source solution by fitting the synthetic seismograms to the observed data

269   considering a regional velocity model (Herrmann et al., 2011). We used the broad-band velocity

270   waveforms, filtered in a frequency band 0.05-0.1 Hz with a length of 120 seconds, recorded at

271   12 seismic stations within 150 km from the earthquake epicenter. We evaluated the source

272   depth by finding iteratively the solution that yields the largest variance reduction (keeping the

273   same observed data). The percentage of double couple component (fixing to zero the

274   volumetric component in the TDMT algorithm) of the moment tensor solution is estimated,

275   additionally, varying and testing different source depths with a sampling of 500 m (for more

276   details, see supplementary material).

277   Given the small expected rupture length, it is important to determine the location of the

278   earthquake rupture nucleation point with the highest possible level of accuracy. Indeed, the

279   preliminary solution (considering a 1D-velocity model, Capuano et al., 2015) available from the

280   probabilistic location method NNLOC (Lomax et al., 2000) and using the first P- and S-arrivals at

281   inland stations at local and regional distances (maximum distance equal to 5.6 km) provided a

282   relatively large error volume ellipsoid (axis lengths of 4 and 2 km, respectively) associated with

283   a maximum likelihood epicentre located about 1 km south of station IOCA consistent with the

284   solution given by (De Novellis et al., 2018).

285   As for the velocity model to be used for simulations, we adopted the 1D velocity model

286   available from the literature and used by INGV to locate the earthquakes occurring at Ischia

287 island and in the more large Campi Flegrei area (Capuano et al., 2015). We further refined this

288 4-layer velocity model (Figure S4), by subdividing the shallower 900m thick velocity layer in

289 three further layers with variable thickness, P-velocity and Vp/Vs. In order to estimate the Vp,

290 Vp/Vs and thickness of these shallow layers, we performed a grid-search analysis for the

291 optimal values relying on waveforms that matched the average amplitude, frequency content

292 and duration of the observed horizontal signals.

293 Based on the previous preliminary location, we explored the possible point-source earthquake

294 position as nodes of three circular grids centred at station IOCA and having 600m, 900m and

295 1200m radius respectively, for a total of 24 explored potential source locations (see Figure 3).

296 After preliminary analyses and trial forward modelling, we fixed the depth of the source at 1.1

297 km, moment magnitude Mw 4 and an isosceles triangular source time function with total

298 duration of 1 sec.

299 The synthetic seismograms for point- and line-source kinematic rupture models have been

300 obtained computing numerical Green's functions in the 1D refined velocity model for the Ischia

301 island using the code AXITRA (Coutant, 1990). AXITRA is based on the discrete wave number

302 method (Bouchon & Aki, 1977). This method introduces a spatial periodicity of sources to

303 discretize the radiated wave field, and it is based on the Fourier transform in the complex

304 frequency domain to calculate the Green's functions.

305 For all the initial testing configurations including the 11 different source mechanisms and 24

306 point-source locations in the circular grid around the IOCA station (Figure 3a/c), we run the

307 Powell' inversion method to find the optimum location and mechanism of the rupture initiation

308   providing the minimum cost function value by fitting the observed and synthetic waveforms

309   using a L2 minimum norm criterion. Figure 3 summarizes the results of the first step of our

310   analysis. The best-fit point-source locations are obtained at circular grid nodes in W-NW sector

311   within 600-1200 m epicentral distance from station IOCA, while the preferred focal mechanism

312   solution is a N115° striking (conjugate plane, N227°) thrust fault with a significant right-lateral

313   strike slip component. Figure 3b shows the comparison between the observed (black) and

314   synthetic (red) waveforms for the best point source specified with number 1 in Figure 3a.

315   **3.2 Finite-Fault Model**

316   The obtained source position and mechanism parameters are taken as a reference model for

317   the next step, which assumes an extended linear rupture to invert the whole 4-second duration

318   waveforms in a higher frequency range. In this second modelling step, the preliminary

319   information about the earthquake location, focal mechanism and velocity model inferred by the

320   point-source analysis have been used as prior information to estimate the kinematic

321   parameters of the linear rupture model.

322   It is worth to note that distinguishing between the nodal planes in the case of a point source is

323   not possible, since the cost function values (RMSD or CC) are the same value for both fault

324   planes. However, in the extended source model, the causative fault is possibly distinguished

325   from the auxiliary plane as the associated seismograms and cost function values of each plane

326   are made different by the rupture directivity. As for the line source geometry and orientation,

327   since there is no prior information about the causative fault, both the fault plane solutions

328   derived from the first step of the analysis have been tested in this second step of modelling.

329   The earthquake rupture is set as a line source with 1 km length (e.g. the expected rupture

330   length for an earthquake of magnitude about 4 (Wells & Coppersmith, 1994)) discretized with

331   four point sources, with a spacing of 250m along the line. The final number of sources

332   composing the line and their relative spacing have been chosen after preliminary trials with

333   different point-source spacing, considering the frequency range of the analysis (0.5-3Hz) and

334   realistic values of rupture velocity to avoid the aliasing effect.

335   The slip-rate history at each of the radiating sources along the line is described by an isosceles

336   triangular source-time function with equal duration of 1 second and varying amplitude, related

337   to the point-source seismic moment.

338   We inverted the 0.5-3 Hz band-pass filtered horizontal velocity records at station IOCA using

339   the Powell' method (and same cost functions as for the point-source step i.e., CC and RMSD) to

340   search for the optimal distribution of the seismic moment for each of the considered point

341   sources and uniform rupture velocity ($v_r = \alpha v_s$). In addition, for each of the two fault planes of

342   the previously retrieved point-source mechanism, the location of the point-source originating

343   the rupture was evaluated in the inversion process by considering all sources as a possible

344   rupture nucleation point.

345   For both fault planes of the source mechanism and all rupture models assuming the nucleation

346   at each of the considered point-sources along the line, we run the Powell' inversion starting

347   from 10 initial models with variable seismic moment distribution and average rupture velocity.

348   All the resulting final 80 models (two lines x 4 point-source origin x 10 initial models) have been

349   classified following their cost function values. By comparing only the best-fit cost function

350   (minimum RMSD and maximum CC among 10 initial models) for each point-source assumed as

351   the initiation of the rupture, distinguishing between both nodal planes was not easy relying

352   only on the RMSD values, as the difference between some categories were negligible and we

353   faced a multi-minima problem. While the CC parameter played an important role to find the

354   optimum model among all explored configurations as it is shown in Figure 4c. This figure

355   represents the maximum CC for each point-source as the nucleation of the rupture.

356   To evaluate the cost function of the Powell' inversion method, we calculated the synthetic

357   seismogram using the code AXITRA that has already been used for the first modelling step.

358   During all simulation steps, the comparison between the observed and synthetic seismograms

359   is done using a time window starting from the P-wave onset, which is picked manually for

360   observed records and automatically for synthetic signals with theoretical arrival time estimated

361   by TauP Toolkit (Crotwell, et al., 1999). To avoid any error in picking the P-arrival time, the

362   alignment of observed and synthetic signals is also controlled by computing the signal cross

363   correlation and shifting the signals accordingly when this value exceeded the threshold value of

364   0.2 seconds.

365   Therefore, among the 80 explored configurations along both nodal planes and assuming the CC

366   parameter as a best cost function provided the best waveform misfit, the optimum line-source

367   of this event is modelled as it is shown in Figure 4a.

368   The retrieved best-fit line-source model shows a bi-lateral (origin at the second point source

369   from the north-western end) rupture propagation with a constant rupture velocity, 75% of the

370   average shear wave velocity within shallower first km layers. Figure 4b presents the comparison

371   between the observed and synthetic waveforms inverted using finite dimension fault model.

372   **4 Discussion**

373   *Fault mechanism and rupture model*

374   The 2017 Ischia earthquake has been recorded by the three-component accelerometric station

375   IOCA located at a near-source epicentral distance (< 1 km) showing a low-frequency, large

376   amplitude ground shaking and long lasting (about 4 seconds) S- and surface-wave signal much

377   longer than the expected source duration of similar size (Mw ~4) events recorded worldwide

378   (Wells & Coppersmith, 1994). This unusual amplification and time duration of the earthquake

379   signal can be interpreted as the combined effect of a shallow propagating rupture and multi-

380   path wave phenomena due to a low-velocity waveguide caused by the shallow trapping

381   geological structures such as alluvial valleys, sedimentary basins or, as in this case, recent

382   volcanic deposits (Foda et al., 1995; Di Giuseppe et al., 2017; Sbrana et al., 2009; Penta &

383   Conforto, 1951). Using a trial and error modelling of the low-pass filtered IOCA record, we

384   refined the initial INGV velocity model including a fine sub-structuring of the shallower layer,

385   with a   80m thick very low P-velocity (400 m/s) layer, lying above a   400

386   m thick, high-velocity (1000 m/s) layer, which allows us to properly reproduce the

387   clear signal reverberation, about 4-second long, in the ground velocity time series.

388   Although the near field waves are often ignored in the earthquake modelling to calculate the

389   synthetic seismograms, similar to the work done by Legrand & Delouis (1999), we demonstrate

390   that these near field signals provide important information to constrain the fault plane also if

391   only one station is available, both in the case of point source and finite extended source

392   models. Since the amplitudes of the near field waves with source to receiver distance (r) decay

393   as 1/r2, a small change in distance implies a larger change in amplitude and then provides a

394   sharp restriction on the orientation of the fault (Legrand et al., 1999; Legrand & Delouis 1999).

395   Nevertheless, even considering the smallest considered frequency range for our modelling (0.5

396   Hz), the observation distance remains 2-3 times greater than the S-dominated signal.

397   The inversion of the 0.5 Hz low-pass filtered horizontal-velocity waveforms at IOCA, assuming a

398   point-source approximation of the earthquake rupture, indicates that it nucleated at an

399   approximate depth of 1 km, and at an epicentral distance of 600 meters west of the IOCA

400   station.

401   All the fault plane solutions for the 2017 Ischia earthquake, computed in this study with

402   different methodologies and observed data, are compatible with a thrust kinematics and are

403   consistent with the same tectonic regime (see supplemental material). In fact, according to the

404   P- and T-axes plunges, ranging between 4°-32° and 47°-79° respectively, the focal mechanism

405   solutions correspond to thrust or thrust-strike slip faulting (Zoback, 1992) with a rotation of

406   nodal planes according to the rake angle.

407   The total released seismic moment is estimated to be $2.5 \times 10^{15} \, Nm$ which corresponds to a

408   moment magnitude of $M_w 4.2$. If we consider an approximate rupture surface of $1000 \times 1000 \, m^2$

409   and a local rigidity $\mu = 2.2 \, GPa$ ¿ this gives an average slip at the fault of $1.1 \, m$ and a static stress-

410   drop $\Delta\sigma = 3.5\,MPa$. The latter is computed using the average slip solution for shear crack under

411   a uniform stress drop ($\Delta u = C\dfrac{\Delta\sigma}{\mu}W$, C=0.728, W=1000m) (Madariaga ,1977).

412   *Simulated shake map and observed macroseismic intensity field*

413   In order to check the consistency of the retrieved source model with the observed earthquake

414   impact in terms of ground motion intensity, we simulated the ground motion velocity wavefield

415   generated by the line-source model derived from the fitting of the waveforms at station IOCA.

416   3Hz low pass-filtered, synthetic velocity waveforms have been computed at a dense, regular

417   grid of virtual nodes covering the topographic surface of the island of Ischia. Figure 5 shows

418   that the computed PGV areal distribution has a main NW-SE elongation with predicted highest

419   values of 18-21 cm/sec possibly recorded in the proximity of the station.

420   To compare the predicted PGV map with the observed earthquake damage scenarios, we

421   converted the interpolated iso-contours of EMS-98 macroseismic intensity provided by Del

422   Gaudio et al. (2019) in PGV using the Faenza & Michelini (2010) empirical relationship (Figure

423   5). The synthetic and EMS-intensity derived PGV maps match well showing a similar areal

424   pattern, consistent co-located high observed values and decaying amplitude trend with

425   distance from the finite fault source region.

426   *Comparison of predicted vs observed GPS co-seismic displacement*

427   Comparing the GPS data with the co-seismic displacement fields obtained with the retrieved

428   source model of the 2017 Ischia earthquake, five stations (AQMO, FORI, MEPO, OSCM, SANT)

429   show the same vertical orientation of the computed displacement and other five stations

430   (AQMO, MEPO, OSCM, SANT, SERR) are consistent with the horizontal one (Figure 6) (see

431   supplemental material). On the contrary, 2 stations are opposite or not coincident with vertical

432   (ISC, SERR) and horizontal (FORI, ISCH) displacement. Despite the same orientation for the most

433   of GPS data, the magnitude of the displacement seems to be less constrained at the single

434   stations. It is worth noting that most of the GPS data show an error greater than their (vertical

435   or horizontal) records and only 2 stations (MEPO and OSCM) display a considerable offset (> 10

436   mm). In fact, the observations at MEPO and OSCM (co-located with the IOCA seismic station),

437   confirm the validity of the horizontal direction of the modeled coseismic displacement.

438   Moreover, interpolating its vertical component by the cubic spline algorithm, the maximum

439   offset is located close to maximum movement evidenced by the DinSAR data with a comparable

440   magnitude. Our coseismic modelling obtained following Okada (1992) confirms the maximum

441   vertical and horizontal displacements equal to 34 mm and 24 mm, respectively, that are in good

442   agreement with the 40 mm displacement detected during the 2017 Ischia earthquake by the

443   DinSAR (De Novellis et al., 2018, Figure 3). The discrepancy of the average fault slip used in

444   Okada modelling (0.13 m) with the slip as inferred from the kinematic rupture model (1 m) is

445   related to the different fault area and local rigidity selected in the two models (

446    $A_1 = 2.30 \times 10^6 \, m^2$ - $\mu_1 = 7.02 \times 10^9 \, N/m^2$; $A_2 = 1.0 \times 10^6 \, m^2$ - $\mu_2 = 2.02 \times 10^9 \, N/m^2$, respectively).

447   For more details on the ground displacement modeling, see supplementary material.

448   *Possible contribution of earthquake-induced landslides to the detected DinSar ground*

449   *displacements*

450 In Figure 6b/c, we report the maximum displacement retrieved by our coseismic displacement

451 modelling (vertical and horizontal components) and by DInSAR data (vertical component, De

452 Novellis et al., 2018) which are included within the larger area of widespread land-sliding

453 occurred during past historical earthquakes (Rapolla et al., 2010). Most of the strong historical

454 earthquakes have occurred in the northern- northwestern- area of the island and near the

455 village of Casamicciola and, as seismic induced effect, they have triggered slope instability and

456 landslide phenomena as demonstrated by morphological surveys, historical reports and

457 archeological evidences (Mele & Del Prete, 1998). The strongest earthquake occurred in 1883

458 (I0 = X MCS) produced several landslides in the northwestern sector of Ischia causing a severe

459 damage also with its secondary effects (Rapolla et al., 2010). Our coseismic displacement

460 modelling predicts roughly the same maximum vertical displacement ($\sim$ 40 mm) and the same

461 area (its spatial location and dimension), but opposite direction of movement as detected by

462 DInSAR data (downward, De Novellis et al., 2018). So, our results point out that a combined

463 effect of co-seismic maximum displacement with dynamic solicitation and soil compaction

464 caused by low frequency surface wave propagation, can explain the high amplitude vertical

465 displacement observed by DInSAR in the northwestern area of Ischia, where historical

466 earthquake occurred and seismic-induced landslide susceptibility is particularly high.

467 *The 2017 earthquake mechanism and its relation to caldera resurgence mechanisms*

468 Large rock and debris landslides can be originated on Ischia island with different mechanism,

469 extension, and temporal evolution (Selva et al., 2019). Large rock mass deformation can

470 develop over a long-time period (100 years) producing mass rock creep (Chigira 1992) that,

471 accelerated by an external forcing such as earthquake or eruption, may originate landslides. As

472 documented by Della Seta et al. (2012, 2015), the NW sector of Monte Epomeo is affected by

473 an ongoing rock mass creep that originates a slope deformation over an area of about 1.6 km2

474 and is controlled by the mechanical behaviour of the Green Tuff (Marmoni et al. 2017) involving

475 about 190 million m3 (Della Seta et al., 2015, Selva et al., 2019). The 2017 Ischia earthquake

476 induced, as secondary effects, several landslides such as rock falls and shallow earth-slides

477 (Nappi et al., 2018; GdL_DST-CentroMS 2018) close to Casamicciola (Figure 1). Looking at our

478 results, we argue that the 2017 Ischia earthquake triggered a downward rock mass movement

479 in the NW sector of Monte Epomeo resurgent block and, acting as external force, accelerated

480 the ongoing slope deformation consisting in a probably long-time creeping of rock mass in the

481 area. So, under this hypothesis, the DInSAR data could have documented a downward

482 movement that does not correspond to the direct co-seismic fault slip (upward), but rather to a

483 combined effect of coseismic offset and slope instability as induced effect.

484 As evidenced by the calculated normal fault plane solution (De Novellis et al., 2018; Nappi et al.,

485 2018), several authors (Trasatti et al., 2019; De Novellis et al., 2018) suggested that 2017 Ischia

486 earthquake is consistent with a deflationary mechanism due to magma degassing from a

487 cooling magma body. A slow subsidence has been supposed active and continuous at Ischia for

488 the last centuries as recently recorded by GPS and DInSAR data (De Martino et al., 2011; Manzo

489 et al., 2006; Castaldo et al., 2017). Nevertheless, the source modelling of 2017 Ischia

490 earthquake retrieved in this study seems to be not consistent with a deflationary/subsidence

491 mechanism. In fact, the earthquake location, the fault geometry, the kinematics, and the

492 surface coseismic displacement suggest that the earthquake activated a reverse dipping-inward

493 fault according to a resurgence mechanism of Monte Epomeo block. Although proving that the

494 caldera resurgence is still active or not at Ischia is beyond the scope of this work, we think that

495 it cannot be completely excluded as evidenced by our results. Several reasons can be brought

496 to support our hypothesis:

497 1.   Ischia magmatic system is still active and recent volcanic activity of the island was

498 strongly influenced by the resurgence mechanism whose rest is not fully proved

499 2.   Structural and volcanological evidences show that the caldera resurgence was

500 discontinuous, episodic, and asymmetrical (i.e. restricted): it was accommodated by reverse

501 dipping-inward fault system mostly at the NW-border of Monte Epomeo block.

502 3.   The extensional regional stress field, as evidenced by GPS and DInSAR measurements, is

503 not in contrast with a local stress field of the resurgence block, that in the NW sector of the

504 island may locally allow the asymmetrical uplift of the Monte Epomeo, as proved by the

505 volcanic activity of the last 33 ka

506 4.   The subsidence of the Ischia island should be widespread and favoured by a normal

507 outward-dipping fault system like those mapped and surveyed at the borders of Monte

508 Epomeo, not only concentrated at its NW- sector. On the contrary, the 2017 Ischia earthquake

509 is modelled by an inward dipping normal fault, despite the existence of a fault system with

510 opposite dip and the presence of N-, NE-dipping coseismic fractures, as pointed out by some

511 authors (Nappi et al., 2018).

512 5.   Ischia is a complex active volcanic system in which different mechanisms (volcanism,

513 earthquake, and slope instability) may occur with different temporal evolution and spatial

514   extent. Their interactions may produce different local stress field and surface deformations that

515   can be misinterpreted when GPS or DInSAR data are measured.

516   Our source model is therefore compatible with a shallow earthquake located near the border of

517   caldera resurgent block (probably still active) where mass rock creep evolved into widespread

518   collapses, recorded by Dinsar data, at NW of Monte Epomeo. In addition, this retrieved model

519   well fits a possible natural hazard scenario proposed for the Ischia volcano (Selva et al., 2019).

520   **5 Conclusions**

521   The analysis and modelling of seismic, geodetic, and structural geological data related to the

522   2017 M 4.2 (the magnitude determined in this study) Ischia earthquake allows to draw the

523   following summary conclusions:

524   -   The earthquake rupture nucleated at an approximate depth of 1 km, and at an

525   epicentral distance of 600 meters west of the IOCA station along a NW-SE, 1 km long,

526   rupturing plane (e.g. the NW-SE trending plane of the point-source mechanism

527   solution). The rupture propagated bi-laterally at an approximately constant rupture

528   velocity of 650 m/s, (60% of the average shear wave velocity within the first km layer).

529   Assuming an approximate rupture surface of $1000 \times 1000\, m^2$ and a local rigidity

530        $\mu = 2.2\, GPa$ ¿this gives an average slip at the fault of $1.1\, m$ and a static stress-drop

531        $\Delta\sigma = 3.5\, MPa$·

532   -   All our fault plane solutions for the 2017 Ischia earthquake are consistent with a thrust

533   kinematics and the same tectonic regime. The P- and T-axes plunges range between 4°-

534   32° and 47°-79° respectively, with the focal mechanism solutions corresponding to

535   thrust or thrust-strike slip faulting (Zoback, 1992) with a rotation of nodal planes

536   according to the rake angle.

537   -   The computed PGV areal distribution has a main NW-SE elongation with predicted

538   highest values of 18-21 cm/sec possibly recorded in the proximity of the station. This

539   pattern well matches the observed earthquake damage scenarios, as reproduced by iso-

540   contours of EMS-98 macroseismic intensity converted in in PGV. The synthetic and EMS-

541   intensity derived PGV maps show a similar areal pattern, consistent co-located high

542   observed values and decaying amplitude trend with distance from the finite fault source

543   region.

544   -   The comparison of the GPS data with the co-seismic displacement field obtained with

545   the retrieved source model of the 2017 Ischia earthquake shows a good consistency

546   with vertical and horizontal orientation of the computed displacement while the

547   absolute amplitude is less constrained. Our coseismic modelling confirms the maximum

548   vertical and horizontal displacements equal to 34 mm and 24 mm, are in good

549   agreement with the DinSAR detected 40 mm displacement.

550   -   Our coseismic displacement modelling predicts the same area, a similar amplitude but

551   opposite movement direction with respect to the one derived by DInSAR data. We

552   hypothesize that a combined effect of co-seismic maximum displacement with dynamic

553   wave solicitation/soil compaction can explain the observed displacement by DInSAR in

554   the northwestern area of Ischia, where historical earthquake occurred, and seismic-

555   induced landslide susceptibility is particularly high.

556   -   The source modelling of 2017 Ischia earthquake, that has been retrieved in this study,

557   seems to be not consistent with a deflationary/subsidence mechanism but rather with a

558   resurgence mechanism of the Mt. Epomeo through an activated reverse dipping-inward

559   fault.

560 **Acknowledgements and Data**

567 **References**

568 Acocella, V., & Funiciello, R. (1999). The interaction between regional and local tectonics during

569 resurgent doming: The case of the Island of Ischia, Italy. *Journal of Volcanology and Geothermal*

570 *Research*, 88, 109–123.

571 Acocella, V., Cifelli, F., & Funiciello, R. (2001). The control of overburden thickness on resurgent

572 domes: insights from analogue models. *J Volcanol Geotherm Res*, 111(1):137–153.

573 Acocella, V., & Funiciello, R. (2006). Transverse systems along the extensional Tyrrhenian

574 margin of central Italy and their influence on volcanism. *Tectonics*, 25, TC2003. https://doi.org/

575 10.1029/2005TC001845.

576 Albano, M., Saroli, M., Montuori, A., Bignami, C., Tolomei, C., Polcari, M., et al. (2018). The

577 relationship between InSAR coseismicdeformation and earthquake−induced landslides

578 associated with the 2017 Mw 3.9 Ischia (Italy) earthquake. *Geosciences*, 8(8), 303.

579 https://doi.org/10.3390/geosciences8080303.

580 Azzaro, R., Del Mese S., Graziani L., Maramai A., Martini G., Paolini S., et al. (2017). QUEST-

581 Rilievo macrosismico per il terremoto dell'isola di Ischia del 21 agosto 2017. *Rapporto finale*,

582 *Rapporto interno*, 6 pp., doi 10.5281/zenodo.886047.

583 Bouchon, M. & Aki, K. (1977). Discrete Wave number Representation of Seismic Source Wave

584 Fields. *Bull. Seismol. Soc. Am*, 67, 259–277.

585 Braun, T., Famiani, D., & Cesca, S. (2018). Seismological constraints on the source mechanism of

586 the damaging seismic event of 21 August2017 on Ischia Island (Southern Italy). *Seismological*

587 *Research Letters*, 89(5), 1741–1749. https://doi.org/10.1785/0220170274.

588 Bruno, P. P. G., de Alteriis, G., & Florio, G. (2002). The western undersea section of the Ischia

589 volcanic complex (Italy, Tyrrhenian sea) inferred from marine geophysical data. *Geophysical*

590 *Research Letters*, 29 (9): 1343 doi:10.1029/2001GL013904.

591 Capuano, P., De Matteis, R., & Russo, G. (2015). The structural setting of the Ischia Island

592 Caldera (Italy): first evidence from seismic and gravity data. *Bull Volcanol*, 77, 79.

593 https://doi.org/10.1007/s00445-015-0965-4.

594 Carlino, S., Cubellis, E., Luongo, G., & Obrizzo, F. (2006). "On the mechanics of caldera

595 resurgence of Ischia Island (southern Italy)", Mechanisms of Activity and Unrest at Large

596   Calderas, C. Troise, G. De Natale, C. R. J Kilburn. Geological Society of London,

597   https://doi.org/10.1144/GSL.SP.2006.269.

598   Castaldo, R., Gola, G., Santilano, A., De Novellis, V., Pepe, S., Manzo, M., & Tizzani, P. (2017).

599   The role of thermo-rheological properties of the crust beneath Ischia Island (Southern Italy) in

600   the modulation of the ground deformation pattern. *Journal of Volcanology and Geothermal*

601   *Research*, 344, 154–173. https://doi.org/10.1016/j.jvolgeores.

602   Cesca, S., Rohr A., & Dahm, T. (2013). Discrimination of induced seismicity by full moment

603   tensor inversion and decomposition. *J. Seismol*, 17(1), 147–163. doi: 10.1007/s10950-012-9305-

604   8.

605   Chigira, M. (1992). Long-term gravitational deformation of rocks by mass rock creep.

606   *Engineering Geolog*y, v. 32, p. 157-184.

607   Chiodini, G., Avino, R., Brombach, T., Caliro, S., Cardellini, C., De Vita, S. et al. (2004). Fumarolic

608   and diffuse soil degassing west of Mount Epomeo, Ischia, Italy. *J Volcanol Geotherm Res*,

609   133(1):291–309.

610   Civetta, L., Gallo, G., & Orsi, G. (1991). Sr-and Nd-isotope and trace-element constraints on the

611   chemical evolution of the magmatic system of Ischia (Italy) in the last 55 ka. *J Volcanol*

612   *Geotherm Res*, 46(3):213–230.

613   Coutant, O. (1990). Programme de Simulation Numérique AXITRA, Rapport LGIT, Université

614   Joseph Fourier, Grenoble, France.

615   Crotwell, H. P., Owens, T. J., & Ritsema, J. (1999). The TauP Toolkit: Flexible Seismic Travel-time

616   and   Ray-path   Utilities.   *Seismological   Research   Letters*,   70(2),   154–160.   doi:

617   https://doi.org/10.1785/gssrl.70.2.154.

618   D'Auria, L., Martini, M., Esposito, A., Ricciolino, P., & Giudicepietro, F. (2008). A unified 3D

619   velocity model for the Neapolitan volcanic areas. In W. Marzocchi & A. Zollo (Eds.), Conception,

620   verification and application of innovative techniques to study active volcanoes (pp. 375–390).

621   Roma: Istituto Nazionale di Geofisica e Vulcanologia.

622   De Martino, P., Tammaro, U., Obrizzo, F., Sepe, V., Brandi, G., D'Alessandro, A., et al. (2011). La

623   rete GPS dell'isola d'Ischia: Deformazioni del suolo in un'area vulcanica attiva (1998-2010).

624   Quaderni di Geofisica, 95. (in Italian).

625   De Novellis, V., Carlino, S., Castaldo, R., Tramelli, A., De Luca, C., Pino, N. A., et al. (2018). The 21

626   August 2017 Ischia (Italy) earthquakesource model inferred from seismological, GPS, and

627   DInSAR   measurements.   *Geophysical   Research   Letters*,   45(5),   2193–2202.

628   https://doi.org/10.1002/2017GL076336.

629   De Vita, S., Sansivero, F., Orsi, G. & Marotta, E. (2006). Cyclical slope instability and volcanism

630   related to volcano-tectonism in resurgent calderas: The Ischia island (Italy) case study.

631   Engineering Geology, 86: 148–165.

632   De Vita, S., Sansivero, F., Orsi, G., Marotta, E., & Piochi, M. (2010). Volcanological and structural

633   evolution of the Ischia resurgent caldera (Italy) over the past 10 ky. *Geol Soc Am Spec Pap*,

634   464:193–239.

635 Del Gaudio, C., Aquino I., Ricco C. & Di Vito, M. A. (2019). Ischia volcano: the 30-years-long

636 ground deformation database. PANGAEA, https://doi.org/10.1594/PANGAEA.909710.

637 Della Seta, M., Marotta E., Orsi G., De Vita S., Sansivero F., & Fredi P. (2012). Slope instability

638 induced by volcanotectonics as an additional source of hazard in active volcanic areas: the case

639 of Ischia island (Italy). Bull. Volcanol., 74:79-106, DOI 10.1007/s00445-011-0501-0.

640 Della Seta, M., Esposito, C., Marmoni, G. M., Martino, S., Paciello, A., Perinelli, C., & Sottili, G.

641 (2015). Geological constraints for a conceptual evolutionary model of the slope deformations

642 affecting Mt. Nuovo at Ischia (Italy), Italian Journal of Engineering Geology and Environment, 2.

643 Devoti, R., Martino, P.D., Pietrantonio, G., & Dolce, M. (2018). Coseismic displacements on

644 Ischia island, real-time GPS positioning constraints on earthquake source location. *Annals of*

645 *Geophysics*, 61, 337.

646 Di Giuseppe, M. G., Troiano, A. & Carlino, S. (2017). Magnetotelluric imaging of the resurgent

647 caldera on the island of Ischia (southern Italy): inferences for its structure and activity. *Bull*

648 *Volcanol*, 79(85). https://doi.org/10.1007/s00445-017-1170-4.

649 Di Napoli, R., Martorana, R., Orsi, G., Aiuppa, A., Camarda, M., De Gregorio, et al. (2011). The

650 structure of a hydrothermal system from an integrated geochemical, geophysical, and

651 geological approach: the Ischia Island case study. *Geochem Geophys Geosyst* 12(7).

652 https://doi.org/10.1029/2010GC003476.

653 Dreger, D. S., & Helmberger, D. V. (1993). Determination of source parameters at regional

654 distances with single station or sparse network data. *Journal of Geophysical Research*, 98,

655   8107–8125.

656   Dreger, D. (2003). 85.11 - TDMT_INV: Time Domain Seismic Moment Tensor INVersion.

657   *International Geophysics*, 81, 1627.

658   Faenza, L. & Michelini, A. (2010). Regression analysis of MCS intensity and ground motion

659   parameters in Italy and its application in ShakeMap. *Geophysical Journal International*, 180,

660   1138–1152. doi: 10.1111/j.1365-246X.2009.04467.

661   Foda, M. A., & Chang, Y. H. (1995). Faraday resonance in thin sedimentary layers. *Geophysical*

662   *Journal International*, 123, 559–571.

663   GdL_DST-CentroMS (2018). Relazione finale sui dati risultanti da attività di ricerca condotte nel

664   comune di Forio (Ischia, NA) e validi ai fini degli studi di risposta sismica locale. Convention CNR-

665   IGAG and DST Sapienza (0004010–10/11/2017) prot. 0004286, cfr. Art. 8 OCDPC n. 476/2017.

666   Gillot, P. Y., Chiesa, S., Pasquare, G., & Vezzoli, L. (1982). <33,000-yr K–Ar dating of the volcano–

667   tectonic horst of the Isle of Ischia, Gulf of Naples. *Nature*, 299(5880):242–245.

668   Herrmann, R., Benz, H., & Ammon, C. J. (2011). Monitoring the Earthquake source process in

669   North America. *Bulletin of the Seismological Society of America*, 101, 2609-2625.

670   Iacono, A. (1996). La "Guerra d'Ischia" nel De Bello Neapolitano di G. Pontano Quaderni

671   dell'Accademia Pontaniana.19:1–90.

672   Lancieri, M., & Zollo, A. (2008). A Bayesian approach to the real–time estimation of magnitude

673   from the early P and S wave displacement peaks. *J. Geophys. Res*., 113, B12302,

674   doi:10.1029/2007JB005386.

675   Legrand, D., & Delouis, B. (1999). Determination of the fault plane using a single near-field

676   seismic station with a finite-dimension source model, Geophysical Journal International, 138

677   (3), 801–808. https://doi.org/10.1046/j.1365-246x.1999.00917.x.

678   Legrand, D., Kaneshima, S., & Kawakatsu, H. (1999). Moment tensor analysis of near field

679   broadband waveforms at Aso volcano, Japan, J. Volc. Geotherm. Res. (in press).

680   Lomax, A., Virieux J., Volant, P., & Berge-Thierry, C. (2000). Probabilistic Earthquake Location in

681   3D and Layered Models. In: Thurber C.H., Rabinowitz N. (eds) Advances in Seismic Event

682   Location. Modern Approaches in Geophysics, Springer, 18.

683   Luongo, G., Cubellis, E., Di Vito, M. A., & Cascone, E. (1995). L'isola d'Ischia: dinamica e struttura

684   del M.Epomeo. In: "Cinquanta anni di attività didattica e scientifica del Prof. F. Ippolito". Liguori

685   (ed), Naples, pp 427–436.

686   Luongo, G., Carlino S., Cubellis E., Delizia I., Iannuzzi R., & Obrizzo, F. (2006). Il terremoto di

687   Casamicciola del 1883: una ricostruzione mancata, Alfa Tipografia, Napoli, (in Italian).

688   Madariaga, R. (1977). Implications of stress-drop models of earthquakes for the inversion of

689   stress drop from seismic observations. *Pure Appl. Geophys*., 115, 301-316.

690   Manzo, M., Ricciardi, G. P., Casu, F., Ventura, G., Zeni, G., Borgström, S., & Lanari, R. (2006).

691   Surface deformation analysis in the Ischia Island (Italy) based on spaceborne radar

692   interferometry. *Journal of Volcanology and Geothermal Research*, 151(4), 399–416.

693   https://doi.org/ 10.1016/j.jvolgeores.2005.09.010.

694   Marmoni, G. M., Martino, S., Heap, M., & Reuschlé, T. (2017). Gravitational slope-deformation

695 of a resurgent caldera: New insights from the mechanical behaviour of Mt. Nuovo tuffs (Ischia

696 Island, Italy). *Journal of Volcanology and Geothermal Research*, 345, 1-20.

697 Marotta, E. (2001). Processi deformativi all'interno di caldere risorgenti: analisi strutturale

698 dell'isola d'Ischia e comparazione con altre aree risorgenti. PhD Thesis, University of Naples,

699 Italy. 214 pp.

700 Mele, R., & Del Prete, S. (1998). Fenomeni di instabilità dei versanti in Tufo Verde del Monte

701 Epomeo (Isola d'Ischia, Campania). *Boll. Soc. Geol. Ital*., 117(1), 93-112.

702 Nappi, R., Alessio, G., Gaudiosi, G., Nave, R., Marotta, E., Siniscalchi, V. et al. (2018). The 21

703 August 2017 MD 4.0 Casamicciola earthquake: first evidence of coseismic normal surface

704 faulting at the Ischia volcanic island. Seismol. Res. Lett., 89(4),1323-1334. 10.1785/0220180063.

705 Okada, Y. (1992). Internal deformation due to shear and tensile faults in a half-space. *Bulletin of*

706 *the Seismological Society of America*, 82 (2), 1018–1040.

707 Orsi, G., & Chiesa, S. (1988). The uplift of the Mt. Epomeo block at the island of Ischia, (Gulf of

708 Naples): geological and geochemical constraints. *Eos*, 69 (44), 1473.

709 Orsi, G., Gallo, G., & Zanchi, A. (1991). Simple-shearing block resurgence in caldera depressions.

710 A model from Pantelleria and Ischia. *J Volcanol Geotherm Res*, 47:1–11.

711 Penta, F., & Conforto, B. (1951). Sulle trivellazioni in aree idrotermali per ricerche di vapore. L"

712 ingegnere, Riv. Tecn. Mens. Ass. Naz. Ingg. Archt. It., Milano, 3, 12 (in Italian).

713   Powell, M. J. D. (1983). Variable Metric Methods for Constrained Optimization. In: Bachem A.,

714   Korte B., Grötschel M. (eds) Mathematical Programming. The State of the Art. Springer, Berlin,

715   Heidelberg. https://doi.org/10.1007/978-3-642-68874-4_12.

716   Rapolla, A., Paoletti, V., & Secomandi, M. (2010). Seismically-induced landslide susceptibility

717   evaluation: application of a new procedure to the island of Ischia, Campania Region, Southern

718   Italy. *Eng. Geol.*, 114 (1–2), 10-25. 10.1016/j.enggeo.2010.03.006.

719   Reasenberg, P. & Oppenheimer, D. H. (1985). FPFIT, FPPLOT and FPPAGE; Fortran computer

720   programs for calculating and displaying earthquake fault-plane solutions. *US Geol Surv*, 109, 85–

721   739.

722   Rittmann, A. (1930). Geologie der Insel Ischia, Z. Vulkanol. Ergbon. (6)1–265.

723   Rittmann, A., & Gottini V. (1980). L'Isola d'Ischia- Geologia. Boll. Serv. Geol. Ital., 101: 131–274.

724   Rovida, A., Locati, M., Camassi, R., Lolli, B., Gasperini, P. (eds) (2019). Italian Parametric

725   Earthquake Catalogue (CPTI15), version 2.0. Istituto Nazionale di Geofisica e Vulcanologia

726   (INGV). https://doi.org/10.13127/CPTI/CPTI15.2.

727   Sbrana, A., Fulignati, P., Marianelli, P., Boyce, A. J., & Cecchetti, A. (2009). Exhumation of an

728   active magmatic–hydrothermal system in a resurgent caldera environment: the example of

729   Ischia (Italy). *Journal of the Geological Society*, 166, 1061–1073. doi:10.1144/ 0016-76492009-

730   030.

731   Scognamiglio, L., Tinti, E., & Michelini, A. (2009). Real-time determination of seismic moment

732   tensor for Italian Region. *Bull. seism. Soc. Am.*, 99(4), 2223- 2242.

733 Selva, J., Acocella, V., Bisson, M., Caliro, S., Costa, A., Della Seta, M., & et al. (2019). Multiple

734 natural hazards at volcanic islands: a review for the Ischia volcano (Italy). *Journal of Applied*

735 *Volcanology*. 8, 5 https://doi.org/10.1186/s13617-019-0086-4.

736 Tarquini, S., Isola, I., Favalli, M., Mazzarini, F., Bisson, M., Pareschi, M.T., & Boschi, E. (2007).

737 TINITALY/01: A new Triangular Irregular Network of Italy. *Annals of Geophysics*, 50, 407– 425.

738 Tibaldi, A., & Vezzoli, L. (1997). Intermittenza e struttura della caldera risorgente attiva dell'isola

739 d'Ischia. Il Quaternario. J. Quat. Sci. 10 (2): 465–470.

740 Tonel, G. (2020). Unconstrained optimization using Powell

741 (https://www.mathworks.com/matlabcentral/fileexchange/15072-unconstrained-optimization-

742 using-powell), *MATLAB Central File Exchange*. Retrieved August 6, 2020.

743 Trasatti, E., Acocella, V., Di Vito, C., Del Gaudio, G., Weber, I., Aquino, S., & et al. (2019).

744 Magma degassing as a source of long-term seismicity at volcanoes: the Ischia Island (Italy) case.

745 *Geophysical Research Letters*, 46 (24), 14421-14429. https://doi.org/10.1029/2019GL085371.

746 Vezzoli, L. (1988). Island of Ischia. Quaderni de 'La Ricerca Scientifica'. Consiglio Nazionale

747 Ricerche Roma 114(10):7–126.

748 Wells, D. L., & Coppersmith, K. J. (1994). New empirical relationships among magnitude,

749 rupture length, rupture width, rupture area, and surface displacement. *Bulletin of the*

750 *Seismological Society of America*, 84(4), 974–1002. doi: https://doi.org/.

751 Zoback, M. L. (1992). First and second order patterns of stress in the lithosphere: The World

752 Stress Map Project, J. Geophys. Res., 97(B8), 11703-11728.

753   Zollo, A., & Bernard, P. (1991). How does an asperity break? New elements from the waveform

754   inversion of accelerograms for the 23:19, October 15, 1979 Imperial Valley aftershock, 1991. J.

755   Geophys. Res., 96, 21549–21573.

756
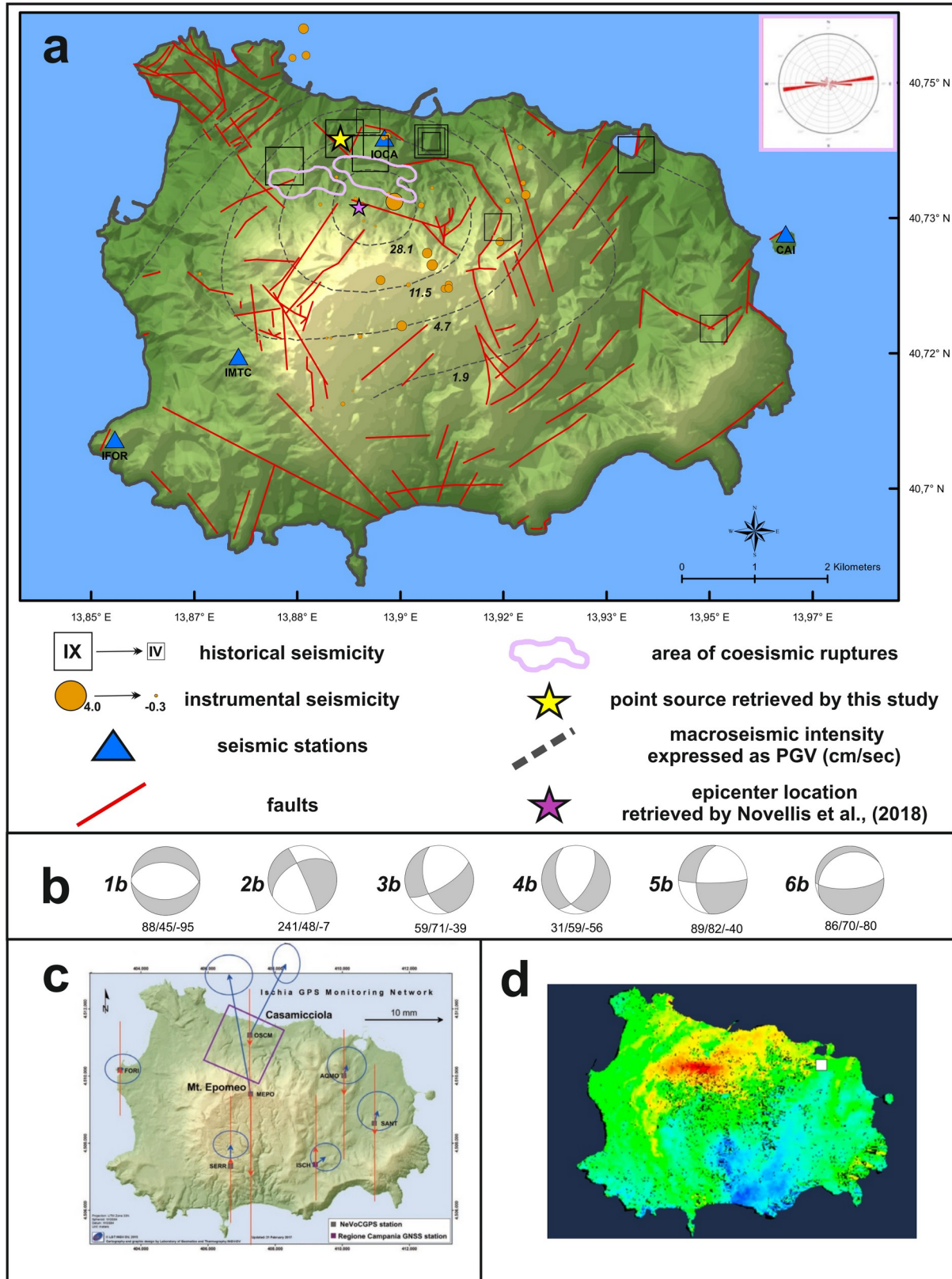
Figure 1. (a) Map of the Ischia island with main structural lineaments (redrawn from De Vita

et al., 2010). Historical (Rovida et al., 2019) and instrumental seismicity (Osservatorio Vesuviano seismic bulletin, earthquake data time span is 2000-2020) is reported with epicenter locations of 2017 Ischia earthquake derived by De Novellis et al. (2018) (violet star) and by this study though the point source modelling (yellow star). Location of the coseismic geological effects of 2017 Ischia earthquake are reported with pink lines with rose diagram indicating the main directions of mapped ruptures (top left). Blue triangles correspond to seismic stations operating on the island. The 10-m-resolution DEM (Tarquini et al., 2007) is represented in the figure. **(b)** Focal mechanism solutions of the 2017 Ischia earthquake computed by different methods from recent works. Keys: 1b=Regional moment tensor by the Saint Louis University, SLU, Herrmann et al. (2011) (http://www.eas.slu.edu/eqc/eqc_mt/MECH.IT/); 2b= Regional Centroid Moment Tensor, RCMT, Pondrelli et al. (2006) (http://rcmt2.bo.ingv.it/); 3b= Time Domain Moment Tensor, TDMT, Scognamiglio et al. (2009) (http://terremoti.ingv.it/tdmt); 4b=Spectral- and waveform-based moment tensor inversions, Cesca et al. (2013) (Braun et al., 2018); 5b=Inversion of focal mechanism by using the P-wave polarities (De Novellis et al., 2018); 6b=Focal mechanism derived by the jointly invertion of t DInSAR displacementand and GPS measurements (De Novellis et al., 2018). **(c)** Map of the coseismic displacement field of the Ischia GPS network with horizontal (blue arrows) and vertical (red arrows) components, from Devoti et al. (2018). The source location obtained from the inversion of GPS data (Devoti et al, 2018) is shown with purple box. **(d)** DInSAR displacement maps computed by CSK images acquired from descending orbits on 19–23 August 2017, from De Novellis et al. (2018).

757
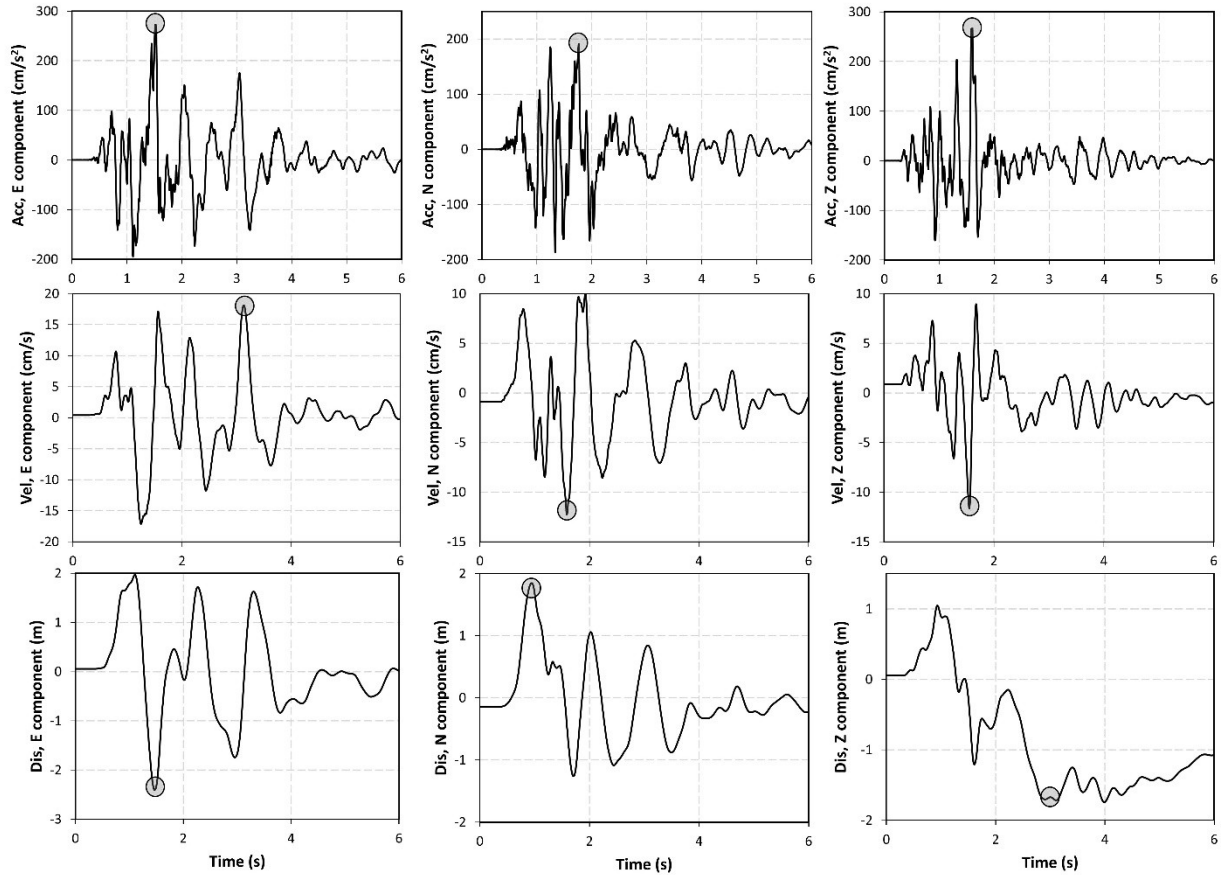
Figure 2. 3-components acceleration waveforms recorded by IOCA station are presented on top-row panels. The middle- and bottom-row panels are velocity and displacement respectively calculated from integration. Circles show the maximum amplitude of each waveform.

758

759

760

761

762
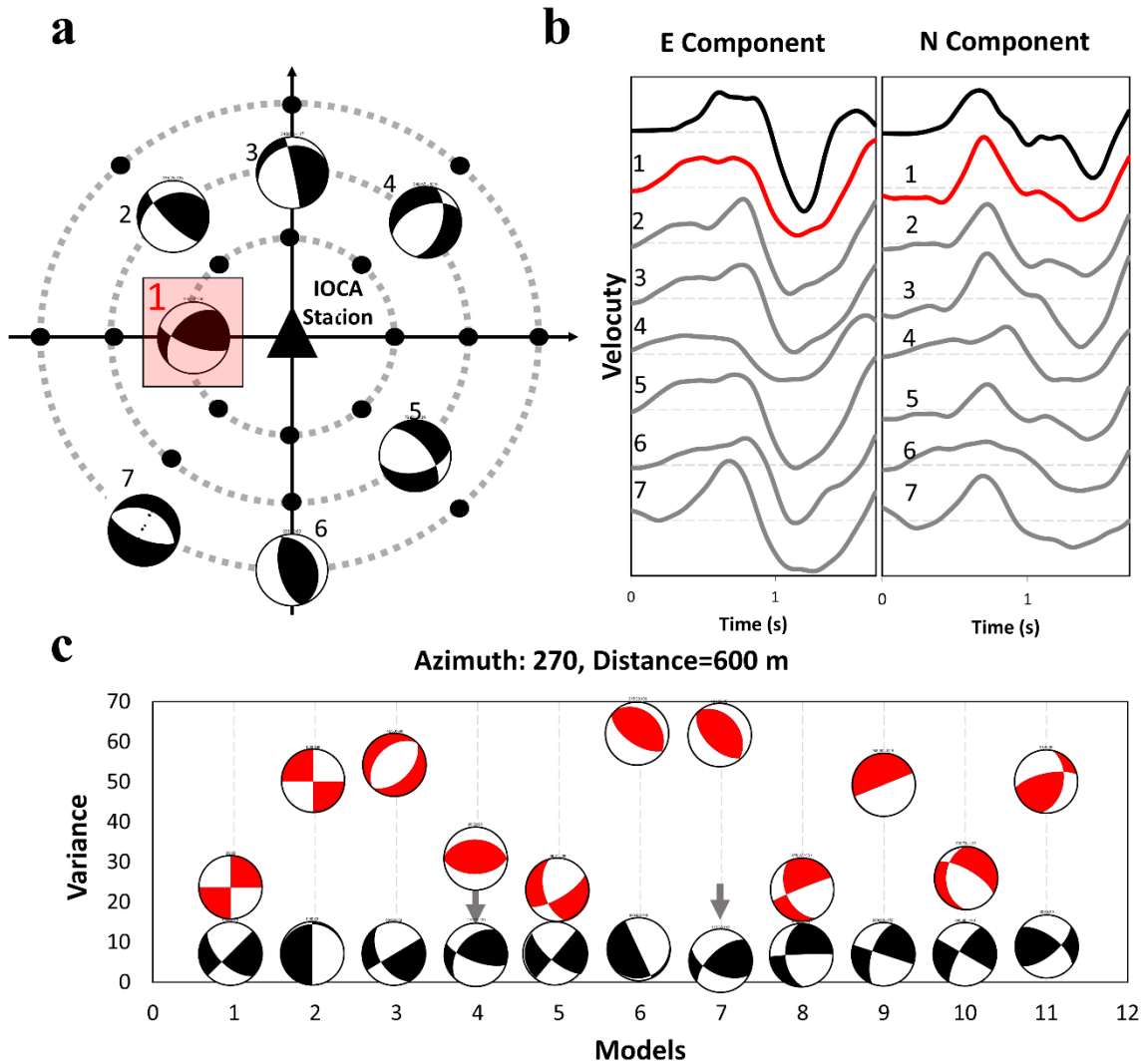
763　**Figure 3. (a)** Schematic map of the point source locations in a circular grid around IOCA used in

764　the first step of the inversion of the complete, three-component waveforms in a time domain.

765　Final focal mechanism of some point-sources is shown as an example. **(b)** Comparison between

766　the observed horizontal velocity waveforms (black) with the synthetic waveforms of the best

767　point source (red) indicated with number 1 in panel a. The gray lines represent the synthetic

768　seismograms for the other numbered locations (from 2 to 7) in panel a. All signals have been

769　aligned from the P-onset and band-pass filtered in the frequency range of (0.05-0.5) Hz. **(c)** This

770   plot shows the output of the Powell inversion method for the best point source (number 1 in

771   panel (a). The black and green beach-balls refer to the initial and final models, respectively.

772

773

774

775

776

777

778

779

780

781

782

783

784

785

786

787

788
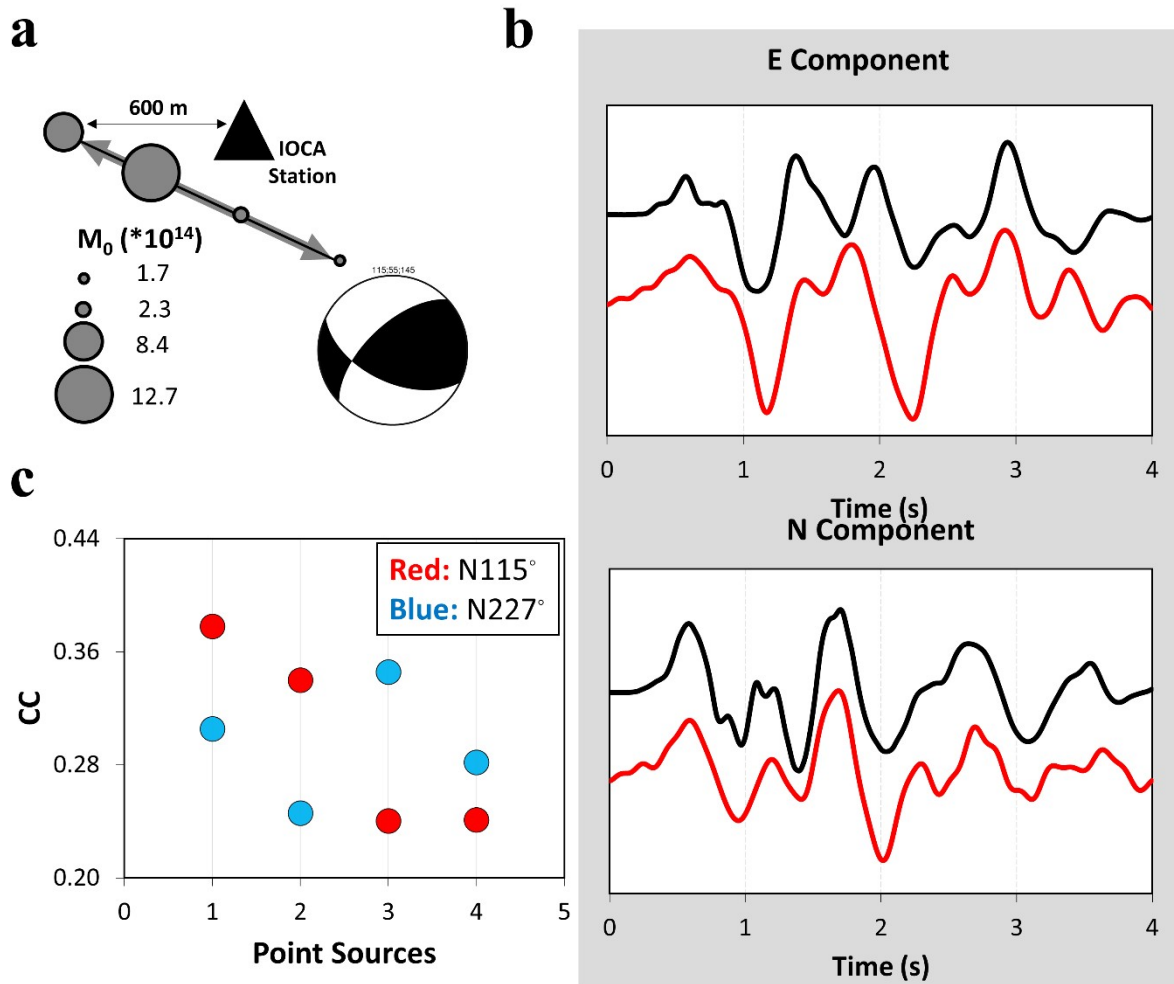
Figure 4. (**a**) The best line-source geometry and orientation (1 km length discretized with four point-sources) with respect to the station IOCA. **(b)** Comparison between the observed and synthetic horizontal velocity waveforms, black and red lines, respectively. Both signals have been band-pass filtered in the frequency range of (0.05-3) Hz and aligned from the P-onset. **(c)** Maximum of CC parameter for each point sources assumed as a nucleation of the rupture. Different colors refer to different nodal planes as written in the legend.

791
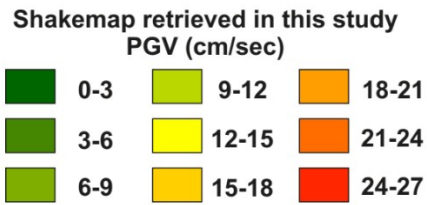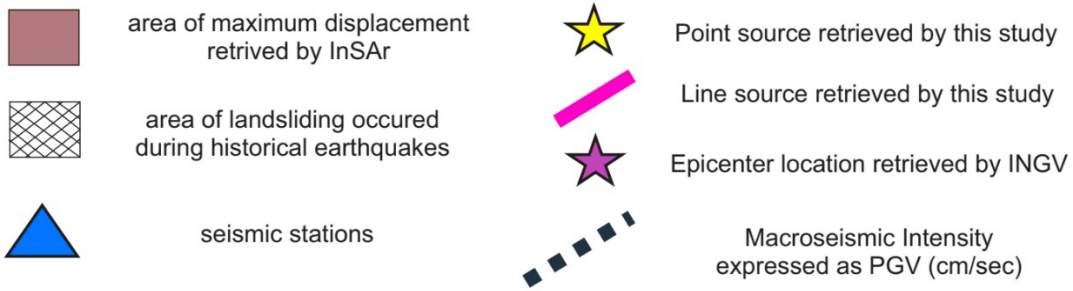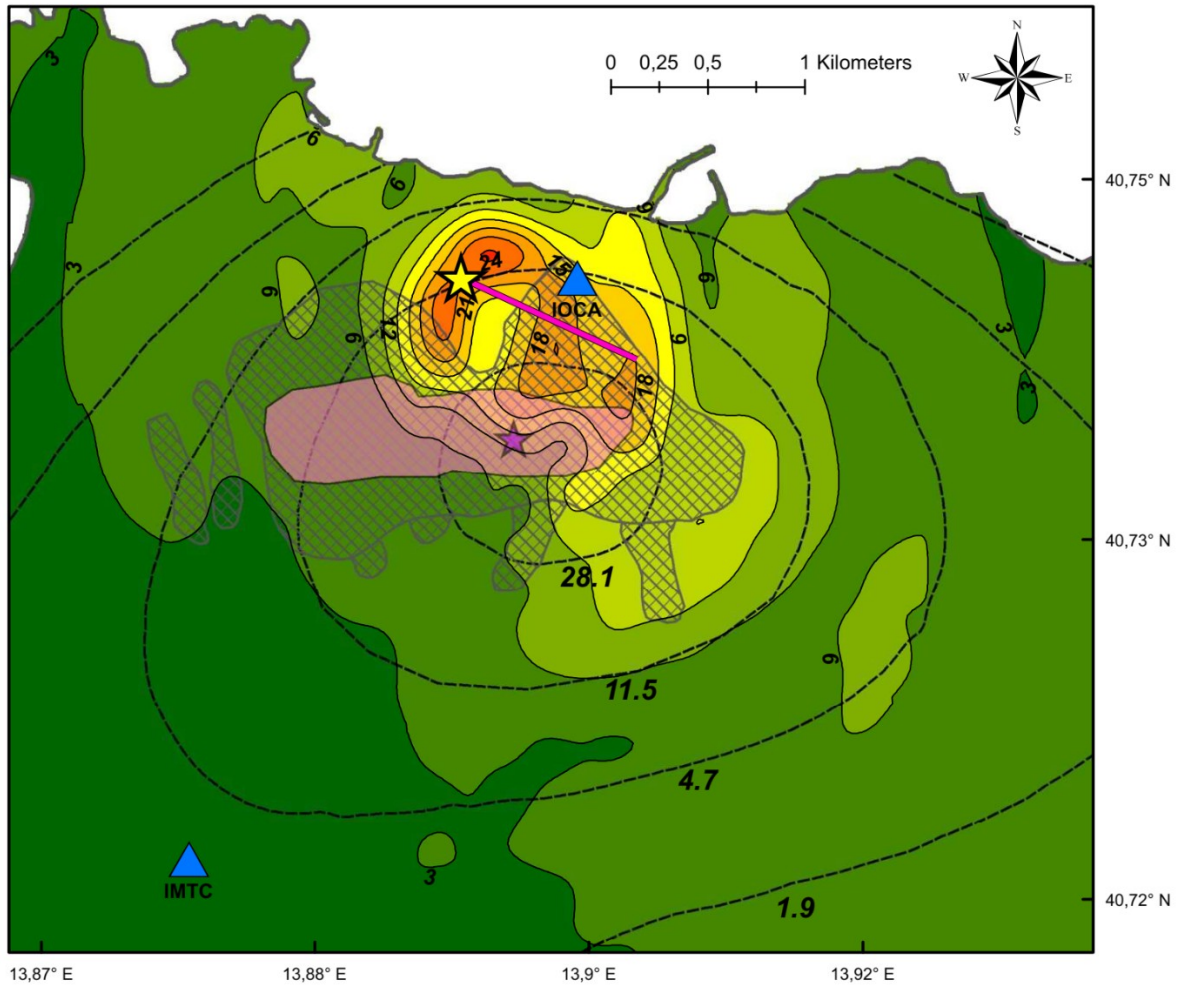
Figure 5. Northern sector of the simulated shake-map calculated for the final rupture model of the 2017 Ischia earthquake together with area of maximum vertical displacement (pink color) from DInSAR data and area of landslides induced by historical earthquakes (reticulate). Macroseismic intensity data, derived from Del Gaudio et al. (2019) and converted in PGV data, are displayed. Line source location derived in this study and epicenter from De Novellis et al. (2018) of the earthquake with IOCA seismic station (blue triangle) are shown.

792

793

794

795

796

797

798

799

800

801

802

803

804

805
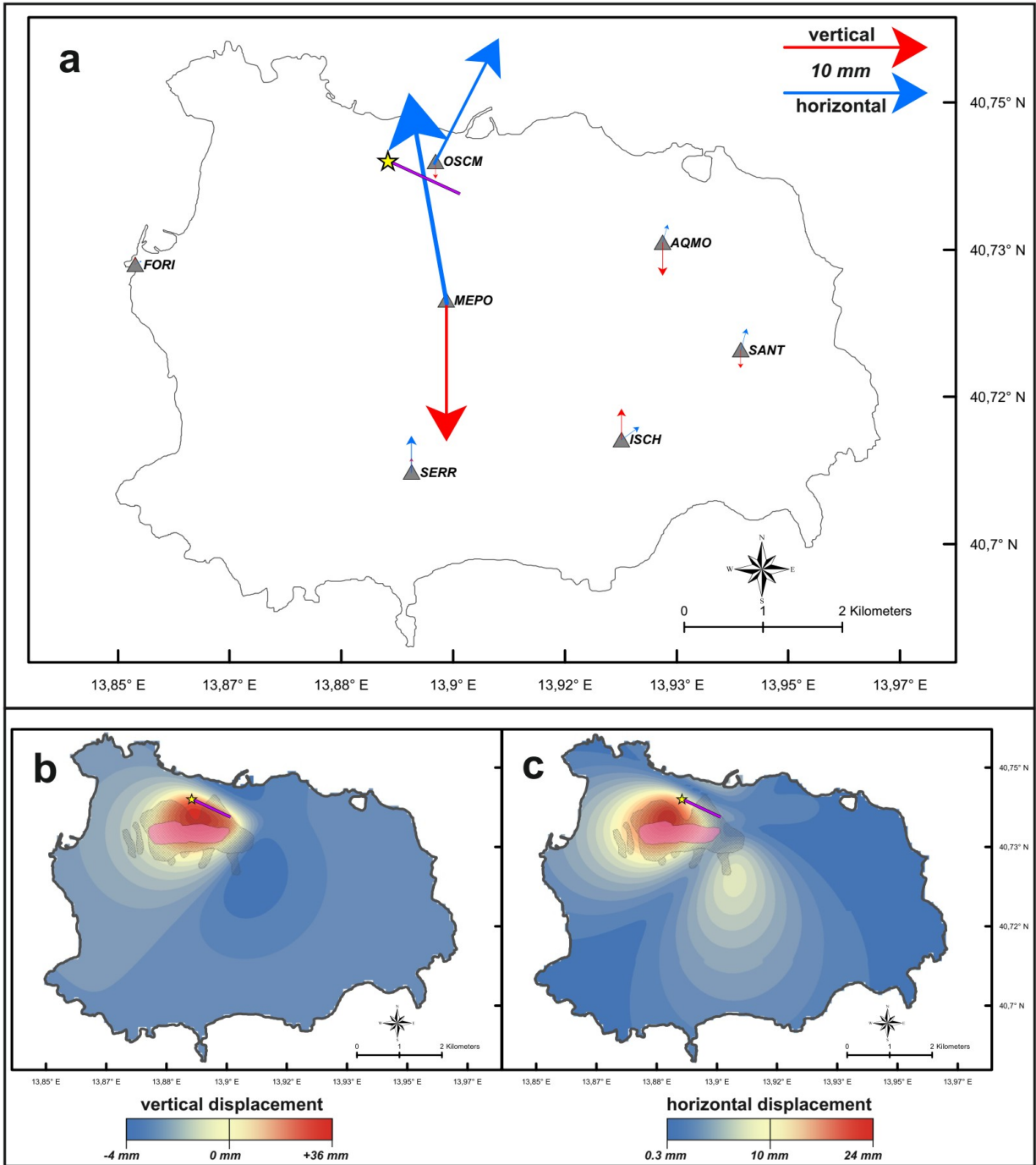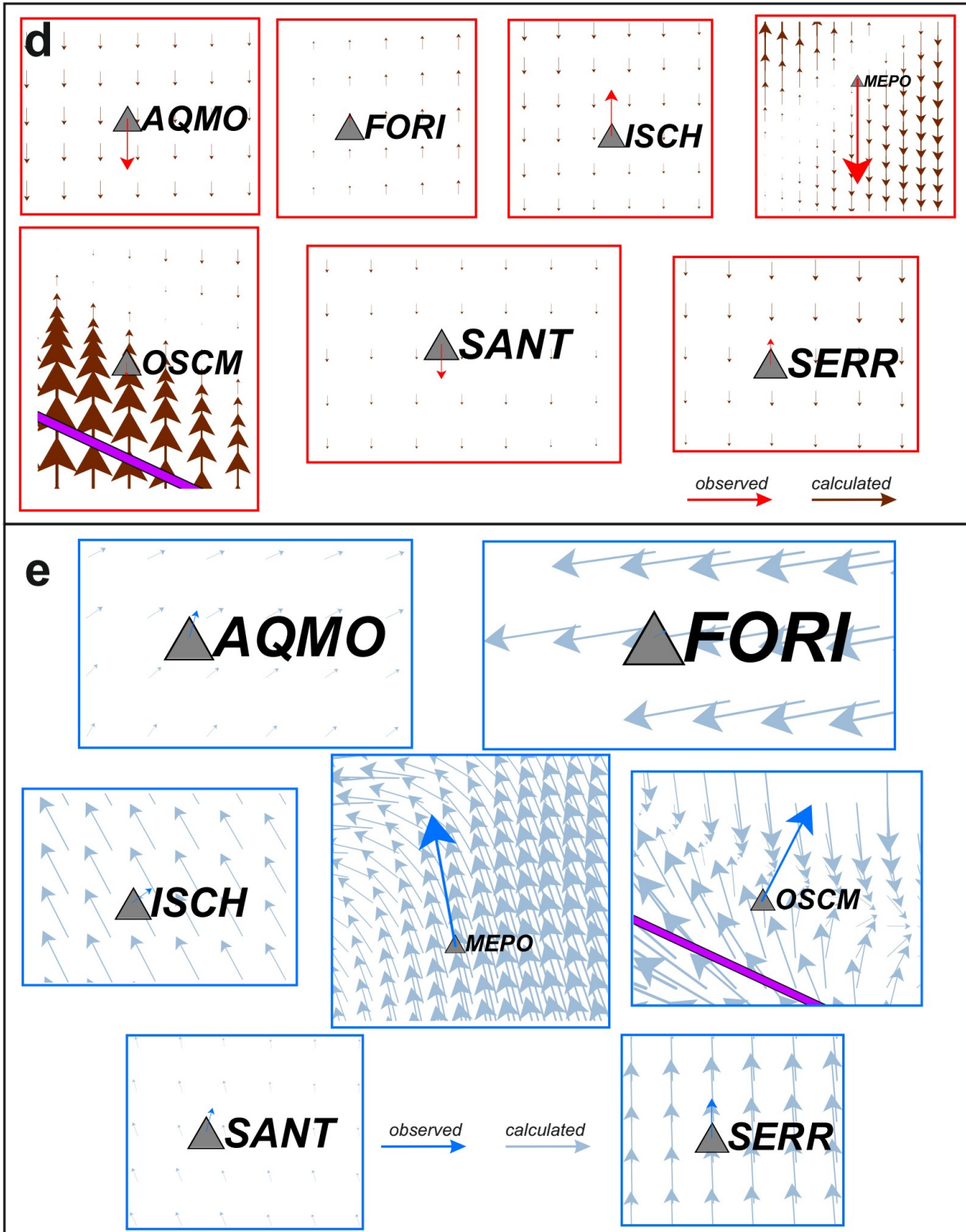
Figure 6. **(a)** GPS measurements and network employed on the Ischia island to detect the coseisimic displacement of the 2017 earthquake. Vertical (red arrows) and horizontal (blue

arrows) components, displayed in the figure, are derived from Devoti at al. (2018). Vertical

(b) and **(c)** horizontal coseismic surface displacement, calculated with Okada (1992) by using

the earthquake source model retrieved in this work, are shown. In figure, maximum

coseismic displacement evidenced by DInsar data (pink area) and area of landsliding occurred

during historical earthquakes (grey area) are reported. In **(d)** and **(e)** a comparison between

GPS data and coseismic surface displacement, as modelled in this study, is displayed for each

GPS station. Both vertical **(d)** and horizontal **(e)** components of field displacement are

calculated.

806